

A Self-Sensing Homopolar Magnetic Bearing: Analysis and Experimental Results

Perry Tsao Seth R. Sanders Gabriel Risk
Department of Electrical Engineering and Computer Science
University of California, Berkeley

Abstract

One of the chief obstacles to constructing a reliable, low-cost, practical magnetic bearing is designing a suitable position sensor. A homopolar magnetic bearing that uses the same coils to stabilize the rotor and sense its position is introduced. A prototype bearing has been built and successfully used to stabilize a rotor. The electromagnetic analysis of the self-sensing function, the implementation of the prototype design, and experimental results verifying the theoretical analysis of the self-sensing scheme are presented in this paper.

1 Introduction

Sensors are a critical element in all active magnetic bearings, but unfortunately, they are costly and frequently represent the weakest point of the system with respect to reliability. As part of an effort to design an economical flywheel energy storage system, a self-sensing homopolar bearing has been designed and developed. In a self-sensing bearing, the same coils used for stabilizing the rotor are also used to sense its position. This eliminates problems with aligning and locating sensors in tightly confined and possibly environmentally hostile areas, reduces cost, and improves reliability by reducing part count and complexity.

An inductive sensing scheme similar in some respects to that described here is discussed in [1]; however the sensor in [1] is not integrated into a self-sensing bearing and uses a sinusoidal carrier rather than a PWM waveform. In addition, the scheme in [1] addresses only sensing along one axis.

In the present paper, the basic principles of operation for a homopolar magnetic bearing, the electromagnetic analysis of the self-sensing scheme, the design of the prototype bearing, and experimental results of the prototype bearing are presented.

2 Principles of Operation

The magnetic flux paths of the prototype bearing are essentially the same as those in a conventional homopolar bearing [2, 3]; however, in our design rotor losses are minimized by using a slotless stator and a toroidal winding scheme. A cutaway view of the bearing is shown in Fig. 1, showing the two stator stacks and the magnet used to provide dc bias flux. Four coils are

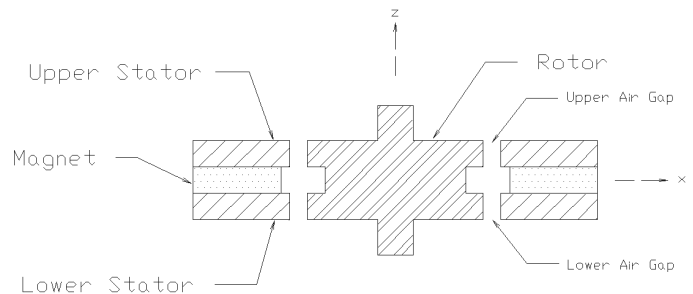


Figure 1: Cutaway view of homopolar magnetic bearing.

wrapped toroidally around each of the stator stacks, with each coil occupying one quadrant. There are two phases on each stator, each consisting of two coils in opposite quadrants, connected in series with their magnetic flux in opposition. Figure 2 shows a cutaway view with the ac and dc flux paths superimposed. For clarity, only the ac control flux path through the upper stator is shown; a similar pattern exists in the lower stator. Force is applied to the rotor when the ac flux reinforces the dc permanent magnet bias flux on one side of the rotor and reduces the field on the opposite side of the rotor. Varying the currents in phases AC and BD controls the direction and magnitude of the ac control flux, and thus the force on the rotor. Since force is proportional to the square of flux density, the bias flux reduces the power needed to operate the bearing.

3 Electromagnetic Analysis of Self-Sensing Operation

The sensing function of the magnetic bearing is analyzed, and it is shown here that position measurement in both axes can be accomplished by sampling voltage at the midpoint of only one of the two phases. Throughout the analysis, variables subscripted with a capital A, B, C, or D indicate values pertaining to coil A, coil B, coil C or coil D, respectively. Subscripts AC or BD indicate values pertaining to the phase AC or phase BD, where phase AC consists of coils A and C connected in series and wound in opposition, and phase BD consists of coils B and D also connected in series and wound in opposition. Definitions for several of the variables are indicated in Fig. 3

The distance between the rotor and the inner diameter of the stator at angle θ , and its corresponding inverse, can be approx-

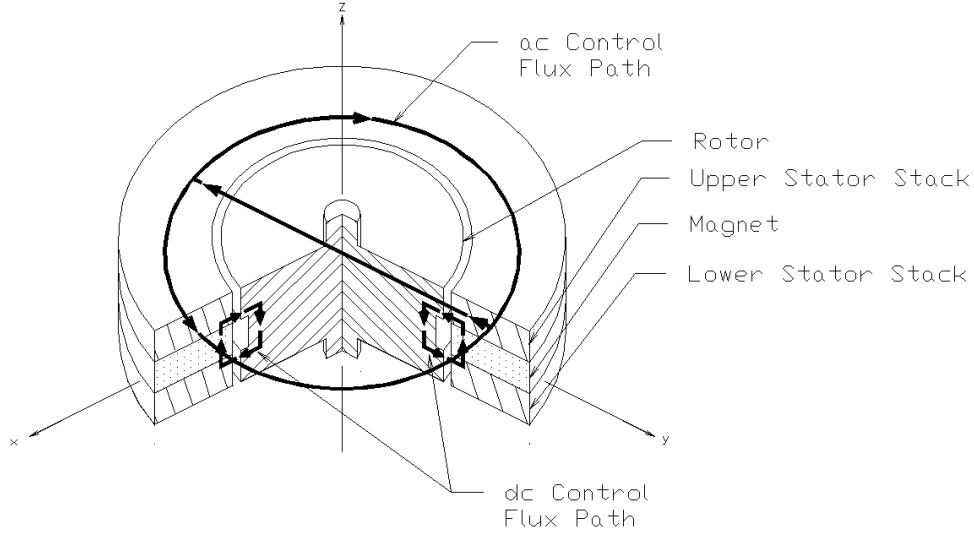


Figure 2: 3D cutaway view showing flux paths.

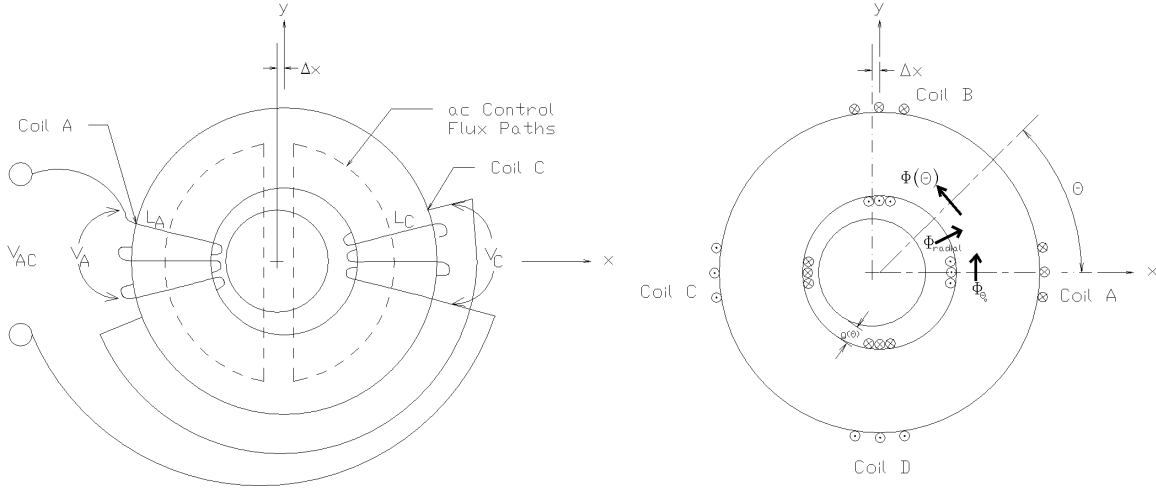


Figure 3: Schematics of stator and coils. For clarity, phase BD and the ac control flux it induces have been omitted in the diagram on the left.

imated to first order as:

$$g(\theta) \approx g_o - \Delta x \cos \theta - \Delta y \sin \theta \quad (1)$$

$$\frac{1}{g(\theta)} \approx \frac{1}{g_o} \left(1 + \frac{\Delta x}{g_o} \cos \theta + \frac{\Delta y}{g_o} \sin \theta \right) \quad (2)$$

where g_o indicates the nominal gap. For ease of analysis, the MMF distribution in the stator is approximated as sinusoidal:

$$MMF_{stator} = MMF_{AC} + MMF_{BD} \quad (3)$$

$$= \frac{N}{2} I_{AC} \sin \theta - \frac{N}{2} I_{BD} \cos \theta \quad (4)$$

where N is the number of turns per coil. To calculate the MMF of the rotor, we first solve for $B(\theta)$, the magnetic flux density

through the gap at angle θ :

$$B(\theta) = \mu_o H(\theta) = \mu_o \frac{MMF_{stator}(\theta) - MMF_{rotor}}{g(\theta)} \quad (5)$$

We then combine (2), (4), and (5), and then solve Maxwell's magnetic flux continuity equation by integrating over the surface of the rotor to find the rotor MMF:

$$0 = \int_0^{2\pi} B(\theta) d\theta \quad (6)$$

$$\Rightarrow MMF_{rotor} = \frac{1}{4g_o} (NI_{AC} \Delta y - NI_{BD} \Delta x) \quad (7)$$

Now to relate the displacements to the inductance, we solve for the flux linkage in each winding. First the flux through a

cross-section of the stator at θ is defined as $\Phi(\theta)$ (consult Fig. 3):

$$\Phi(\theta) = \Phi_{\theta_o} + \int_{\theta_o}^{\theta} \Phi_{radial} d\theta = \Phi_{\theta_o} + \int_{\theta_o}^{\theta} hRB(\theta) d\theta \quad (8)$$

Here h represents the height of the stator, and R its inner radius. The flux linkages for coil A and coil C are then calculated by taking the definite integral of the flux over the length of the winding:

$$\Lambda_A = \frac{N}{\pi} \int_{\frac{\pi}{4}}^{-\frac{\pi}{4}} \Phi(\theta) d\theta \quad (9)$$

$$\Lambda_C = \frac{N}{\pi} \int_{\frac{3\pi}{4}}^{-\frac{3\pi}{4}} \Phi(\theta) d\theta \quad (10)$$

The term $\frac{N}{\pi}$, where N is the total number of turns in the coil, is the turns density. The constant Φ_{θ_o} represents the flux at θ_o , and is canceled out in the definite integral. The resulting flux linkages are:

$$\Lambda_A = \frac{\mu_o h R N^2}{\pi g_o} \left[I_{AC} \left(\sqrt{2} - \frac{\sqrt{2} \Delta y^2}{2 g_o^2} + \frac{1}{4} \frac{\Delta x}{g_o} \right) + I_{BD} \left(-\frac{\sqrt{2} \Delta y \cdot \Delta x}{2 g_o^2} + \frac{1}{4} \frac{\Delta y}{g_o} \right) \right] \quad (11)$$

$$\Lambda_C = \frac{\mu_o h R N^2}{\pi g_o} \left[I_{AC} \left(\sqrt{2} - \frac{\sqrt{2} \Delta y^2}{2 g_o^2} - \frac{1}{4} \frac{\Delta x}{g_o} \right) + I_{BD} \left(-\frac{\sqrt{2} \Delta y \cdot \Delta x}{2 g_o^2} - \frac{1}{4} \frac{\Delta y}{g_o} \right) \right] \quad (12)$$

$$\Rightarrow \Lambda_A - \Lambda_C = \frac{\mu_o h R N^2}{\pi g_o^2} [\Delta x \cdot I_{AC} + \Delta y \cdot I_{BD}] \quad (13)$$

Therefore, the difference in the flux linkages of the two coils in phase AC is proportional to the position of the rotor and the current in phases AC and BD. For now, we neglect the resistive drops to obtain:

$$v_a - v_c = \frac{d(\Lambda_A - \Lambda_C)}{dt} \quad (14)$$

$$= \frac{\mu_o h R N^2}{\pi g_o^2} \left[\Delta x \cdot \frac{dI_{AC}}{dt} + \Delta y \cdot \frac{dI_{BD}}{dt} \right] \quad (15)$$

under the assumption that Δx and Δy change slowly. To first order, the total inductance of phase AC,

$$\Lambda_A + \Lambda_C \approx \frac{2\sqrt{2}\mu_o h R N^2}{\pi g_o} I_{AC} = L_{AC} I_{AC} \quad (16)$$

is constant with respect to Δx and Δy . A similar analysis can be done to obtain $L_{BD} = L_{AC}$. We then substitute $\frac{dI_{AC}}{dt} = \frac{v_{AC}}{L_{AC}}$ and $\frac{dI_{BD}}{dt} = \frac{v_{BD}}{L_{BD}}$ and L_{BD} into (14) arriving at:

$$v_A - v_C = \frac{1}{4\sqrt{2}g_o} [\Delta x \cdot v_{AC} + \Delta y \cdot v_{BD}] \quad (17)$$

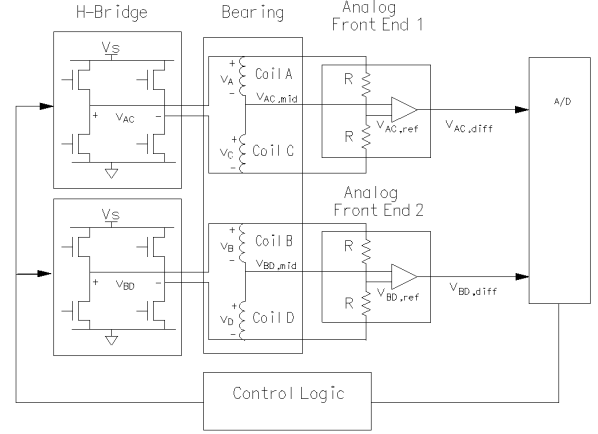


Figure 4: System diagram of prototype.

Thus, it has been shown that to first order the difference in voltage between coil A and coil C is linear with respect to the voltage applied at the terminals of phase AC and phase BD and both displacements Δx and Δy . An analogous result holds for phase BD and $v_B - v_D$.

$$v_B - v_D = \frac{1}{4\sqrt{2}g_o} [\Delta x \cdot v_{AC} + \Delta y \cdot v_{BD}] \quad (18)$$

Sampling the midpoint voltage of phase AC, for example, allows one to deduce the individual coil voltages v_A and v_C . Note that since $v_A - v_C$ contains information on both Δx and Δy it is possible to sense both displacements Δx and Δy by sampling the voltage at only the midpoint of phase AC, or equivalently, by sampling at only the midpoint of phase BD. There are a variety of PWM drive schemes that can facilitate this, but the most straightforward method and the method used in our prototype senses Δx by sampling when $v_{BD} = 0$ and senses Δy by sampling when $v_{AC} = 0$.

The analysis shown here is not limited to bearings with our winding configuration or homopolar bearings. Following the analysis through for bearings with a typical active magnetic bearing winding configuration would lead to similar results. The only restriction is that the opposing coils need to be controlled such that their currents are equal. This requirement is automatically met in bearings where opposing coils are connected in series.

4 Prototype Implementation

4.1 System Overview

A prototype self-sensing bearing was constructed and its self-sensing function has been successfully demonstrated and used to stabilize a 1.5 kg rotor. Fig. 4 shows the components of the system. The diagram shows both phases of the radial bearing, where phase AC controls motion along the y-axis, and phase BD controls motion along the x-axis. In order to remove the common mode signal, an analog differential

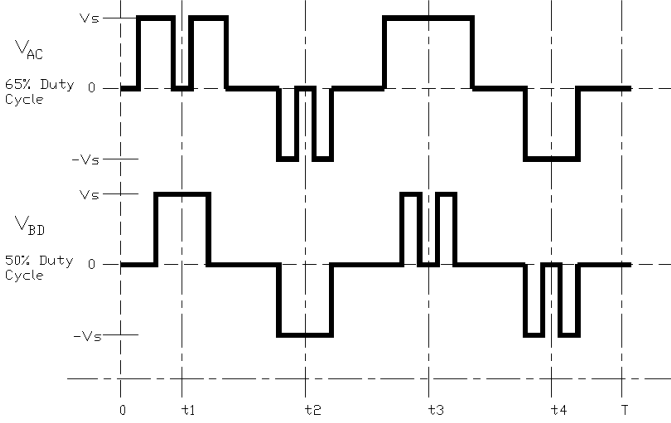


Figure 5: Example PWM waveform.

amplifier was used to compare $v_{AC,mid}$ and $v_{AC,ref}$ to create $v_{AC,diff}$. The amplifier also scaled and biased the signal into the correct range for the A/D converter, which sampled $v_{AC,diff}$. A proportional-derivative (PD) controller and other control logic was implemented using a field programmable gate array (FPGA).

As noted earlier, voltages only need to be sampled at one of the two midpoints, thus only one A/D channel, and one analog front end is necessary. However, as is shown in our diagram, a second sensing channel was implemented in our prototype for testing purposes and to verify our model.

4.2 Error canceling sampling scheme

Example PWM waveforms for v_{AC} and v_{BD} as implemented in our prototype are shown in Fig. 5. Waveform v_{AC} is shown at 65% duty cycle and v_{BD} is shown at 50% duty cycle. Note that v_{AC} is commanded to be zero at times $kT + t_1$ and $kT + t_2$ for all integers k , independent of duty cycle. Likewise, v_{BD} is always commanded to be zero at times $kT + t_3$ and $kT + t_4$.

From inspection of (17), it may seem that the easiest method of sensing position Δy would be to sample $v_{AC,diff}$ at t_1 , and then use the assumption that $V_s = v_A + v_C$ and the fact that $v_{AC,ref} = V_s/2$ to arrive at $v_A - v_C = 2v_{AC,diff}$. However, the assumption that $V_s = v_A + v_C$ ignores resistive drop of the coils, which can be significant since these coils are also used to actuate the bearing.

An intuitive way of understanding how the sensing is affected by the resistance of the coils is to think of the bearing model developed earlier as a black box with two leads from the terminals of each phase and one lead from the midpoint of each phase (see Fig. 6). Placing a resistor in series with each terminal lead will not affect the inductance relationships inside the box, therefore (17) and (18) still hold. However, in this model, when currents are applied, the voltages the bearing model sees are $v_{AC} - i_{AC}(R_A + R_C)$ and $v_{BD} - i_{BD}(R_B + R_D)$, which changes (17) to:

$$v_A - v_C = \frac{1}{4\sqrt{2}g_o} [\Delta x \cdot (v_{AC} - i_{AC}(R_A + R_C))] \quad (19)$$

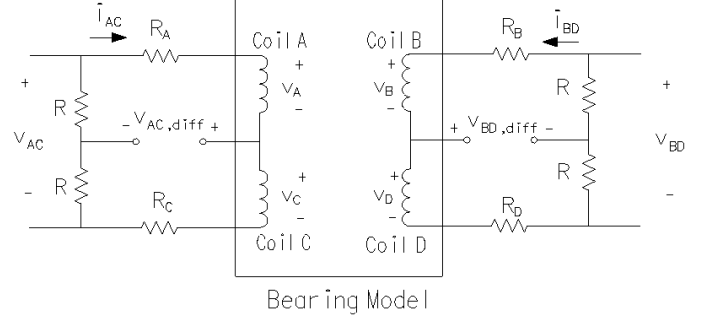


Figure 6: Model of bearing with resistances.

$$+ \Delta y \cdot (v_{BD} - i_{BD}(R_B + R_D))]$$

Clearly, an unwanted current dependence has appeared. However, these currents are associated with stabilizing the rotor and therefore change slowly in comparison to the sampling frequency.

To remove this current dependence in the prototype implementation, $v_{AC,diff}$ is sampled at times t_1 and t_2 . Examining Fig. 6 yields:

$$v_{AC,diff} = \frac{1}{2}(v_C - v_A) + \frac{1}{2}(R_C - R_A)i_{AC} \quad (20)$$

Thus:

$$\begin{aligned} v_{AC,diff}(t_2) - v_{AC,diff}(t_1) &= \frac{1}{2}[v_A(t_1) - v_C(t_1)] - \frac{1}{2}[v_A(t_2) - v_C(t_2)] \\ &\quad + \frac{1}{2}(R_C - R_A)(i_{AC}(t_2) - i_{AC}(t_1)) \end{aligned} \quad (21)$$

To see the current dependence of $[v_A(t_1) - v_C(t_1)] - [v_A(t_2) - v_C(t_2)]$, (19) is evaluated at times t_1 and t_2 , which leads to:

$$\begin{aligned} [v_A(t_1) - v_C(t_1)] - [v_A(t_2) - v_C(t_2)] &= \frac{1}{4\sqrt{2}g_o} \{ \Delta x \cdot [(-i_{AC}(t_1) + i_{AC}(t_2))(R_A + R_C)] \\ &\quad + \Delta y \cdot [2V_s + [(-i_{BD}(t_1) + i_{BD}(t_2))(R_B + R_D)]] \} \end{aligned} \quad (22)$$

Using the assumption that the currents change slowly in comparison to the sampling period implies $i_{AC}(t_1) \approx i_{AC}(t_2)$ and $i_{BD}(t_1) \approx i_{BD}(t_2)$. Then, expression (22) simplifies to:

$$[v_A(t_1) - v_C(t_1)] - [v_A(t_2) - v_C(t_2)] = \frac{1}{2\sqrt{2}g_o} V_s \cdot \Delta y \quad (23)$$

Substituting back into (21) leads to:

$$\begin{aligned} v_{AC,diff}(t_2) - v_{AC,diff}(t_1) &= \frac{1}{4\sqrt{2}g_o} V_s \cdot \Delta y + \frac{1}{2}(R_C - R_A)(i_{AC}(t_2) - i_{AC}(t_1)) \end{aligned} \quad (24)$$

Using the assumption of a slowly changing current again yields:

$$v_{AC,diff}(t_2) - v_{AC,diff}(t_1) = \frac{1}{4\sqrt{2}} \frac{\Delta y}{g_o} \cdot V_s \quad (25)$$

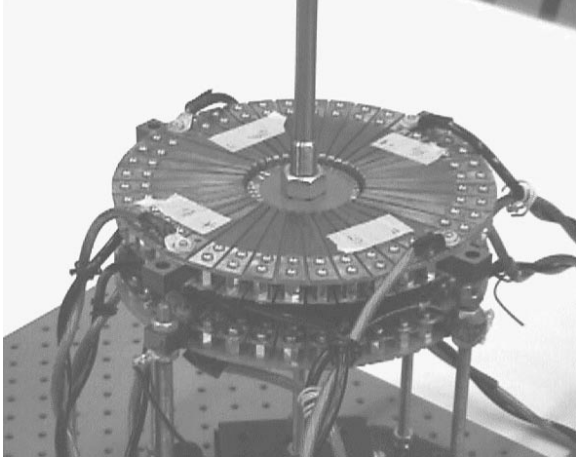


Figure 7: Photo of self-sensing homopolar bearing.

Analogously, the above analysis can easily be modified to show that:

$$v_{AC,diff}(t_3) - v_{AC,diff}(t_4) = \frac{1}{4\sqrt{2}} \frac{\Delta x}{g_o} \cdot V_s \quad (26)$$

Therefore, it has been shown that our self-sensing scheme cancels out errors from resistive drops due to both phase currents i_{AC} and i_{BD} when sensing position along both the x and y axes. By sampling $v_{AC,diff}$ twice and subtracting, not only were the errors in (22) due to the total phase resistance removed, but the errors in (24) due to imbalances of the coil resistances in each phase were also canceled out.

5 Experimental Results

A photo of the prototype appears in Fig. 7., and some parameters for the prototype are presented in Table 1. The prototype was constructed using two stator stacks and two rotor stacks built up from 0.014" M19 steel laminations. The rotor stacks were attached to a solid steel body. A ferrite permanent magnet provided the dc bias flux. The coils were constructed from solid copper pieces bent around the stator stacks. The measured inductance was significantly higher than that predicted by (16) due to leakage inductance. A simple digital controller was implemented with an FPGA.

Some oscilloscope traces of signals in the system are shown in Figs. 8, 9, 10. Fig. 8 shows v_{AC} at its minimum, no-load, 50% duty cycle. The notches cut into the waveform at t_1 and t_2 are approximately $2.5\mu s$ long.

In Fig. 9, the top trace displays a logic output from the controller that indicates whether position data for the x-axis or y-axis is being sampled. The lower trace is $v_{AC,diff}$. Notice how $v_{AC,diff}$ is offset from its nominal voltage at times t_3 and t_4 , which corresponds to a large x-axis displacement. The y-axis displacement is much smaller, therefore at times t_1 and t_2 $v_{AC,diff}$ stays much closer to its nominal voltage.

Fig. 10 shows a closeup of $v_{AC,diff}$ at time t_3 . The $1\mu s$ time period t_s is when the A/D samples $v_{AC,diff}$.

Design values	
Rotor diameter	5.3 cm
Stack height	1 cm
Nominal gap	1 mm (radial)
Laminations	M19 Steel (14 mil)
# Turns/Coil	10
# Coils/Phase	2
PWM switch frequency	20 kHz
Calculated design values	
dc bias field strength	0.8 T
Max. force	500 lbf
Inductance	$30\mu H$
Sensing gain	$2.6V/mm$ at $V_s = 15V$
Measured values	
Inductance of each phase	$62\mu H$
Resistance of each phase	0.091Ω
Sensing gain	$0.75V/mm$ at $V_s = 15V$

Table 1: Self-sensing homopolar bearing design summary.

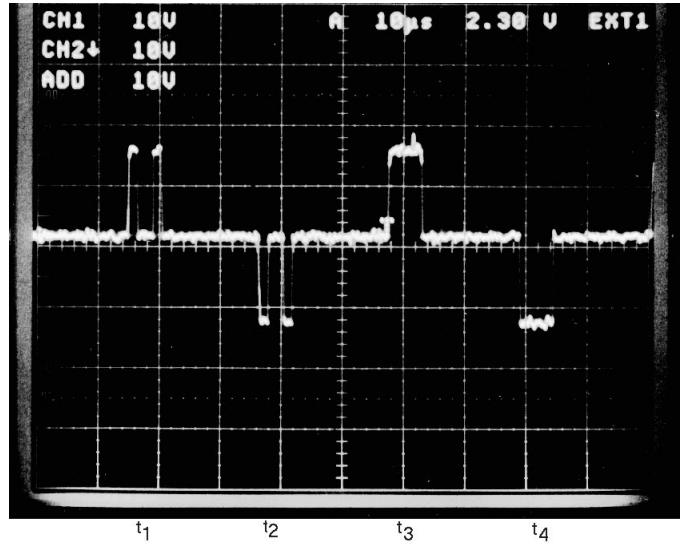


Figure 8: Photo of v_{AC} waveform on oscilloscope.

Data from the self-sensing output is graphed in Fig. 11. As shown in the graph, the outputs of the sensing system, $v_{AC,diff}(t_4) - v_{AC,diff}(t_3)$ and $v_{BD,diff}(t_4) - v_{BD,diff}(t_3)$, are linear with respect to Δx . As is evident from the figure, the response was similar regardless of which phase was sampled, whether it be phase AC at times t_4 and t_3 or phase BD at times t_4 and t_3 .

This agrees with equations (17) and (18) of the analysis, which predicted that the magnitude of the sampled voltage would be linearly proportional to the displacement, and the same on both phases. In addition, no measurable cross-axis coupling was observed, i.e. motion along the y-axis did not influence the x-axis signal, and vice-versa. These observations all agree with our analysis.

The gain of the sensing scheme as shown in Fig. 11 is ap-

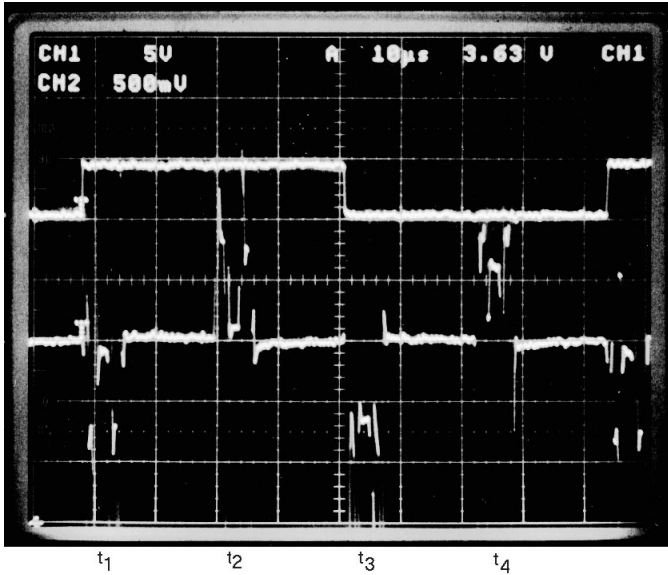


Figure 9: Top trace is logic output indicating whether position data for the x-axis or y-axis is being sampled. Lower trace is of $v_{AC,diff}$.

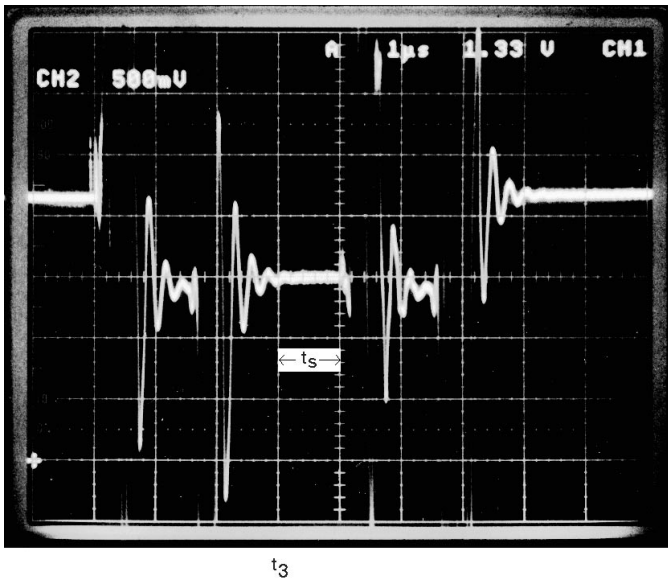


Figure 10: Close up of $v_{AC,diff}$ at time t_3 with sampling time t_s marked.

proximately $0.75V/mm$, and was obtained with $V_s = 15V$. The gain predicted by Eqn. (26) is $2.6V/mm$. The discrepancy is due in large part to the large leakage inductances which reduce the effective voltage on the windings. For example, the measured inductance was more than twice the computed inductance, accounting for at least a factor of two. Other contributing factors may be additional lead inductance, spatial winding harmonics, and three-dimensional effects.

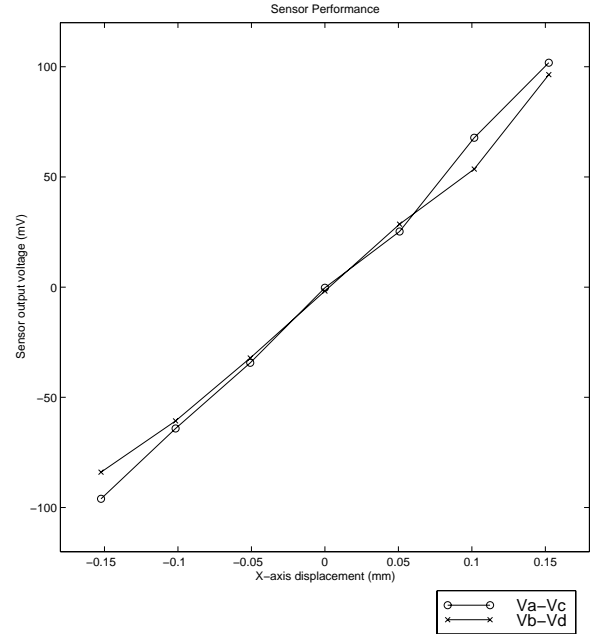


Figure 11: Graph of sensor output versus rotor displacement.

6 Conclusion

A self-sensing homopolar magnetic bearing has been constructed and successfully used to stabilize a rotor radially. An electromagnetic analysis of the self-sensing scheme has been presented, and measurements confirming the analysis and successful operation of the sensor have been described.

References

- [1] T. Haga S. Moriyama, K. Watanabe. Inductive sensing system for active magnetic suspension control. In *6th International Symposium on Magnetic Bearings*, Cambridge, MA, 1998.
- [2] G. Schweitzer, H. Bleuler, and A. Traxler. *Active Magnetic Bearings*. vdf Hochschulverlag, 1994.
- [3] C. Sortore, P. E. Allaire, E.H. Maslen, R.R. Humphris, and P.A.Studer. Permanent magnet biased magnetic bearings-design, construction, and testing. In *2nd International Symposium on Magnetic Bearings*, Tokyo, Japan, 1990.